

Present-day aeolian activity in Herschel Crater, Mars



Marco Cardinale^{a,*}, Simone Silvestro^{b,c}, David A. Vaz^{d,e}, Timothy Michaels^c, Mary C. Bourke^f, Goro Komatsu^g, Lucia Marinangeli^a

^a Laboratorio di Telerilevamento e Planetologia, Dipartimento di Scienze Psicologiche della Salute e del Territorio, Università G. d'Annunzio, Via dei Vestini 31, 66100 Chieti, Italy

^b INAF, Osservatorio Astronomico di Capodimonte, Salita Moiarriello 16, Napoli, Italy

^c Carl Sagan Center, SETI Institute, 189 N. Bernardo Avenue, Suite 100, Mountain View, CA 94043, USA

^d Centre for Earth and Space Research of the University of Coimbra, Observatório Astronómico da Universidade de Coimbra, Almas de Freire, 3040-004 Coimbra, Portugal

^e CERENA, Instituto Superior Técnico, Av. Rovisco Pais, 1049-001 Lisboa, Portugal

^f Department of Geography, Trinity College Dublin, Dublin, Ireland

^g International Research School of Planetary Sciences, Università G. d'Annunzio, Viale Pindaro, 42, 65127 Pescara, Italy

ARTICLE INFO

Article history:

Received 8 May 2015

Revised 12 September 2015

Accepted 26 October 2015

Available online 2 November 2015

Keyword:

Aeolian processes

Mars

Surface

ABSTRACT

In this report, we show evidence for ripple and dune migration in Herschel Crater on Mars.

We estimate an average dune migration of 0.8 m and a minimum ripple migration of 1.1 m in a time span of 3.7 Earth-years. These dunes and ripples are mainly shaped by prevailing winds coming from the north, however we also report the presence of secondary winds which elongate the barchans' horns. Such a complex wind scenario is likely caused by the influence of winds blowing off the western crater rim as suggested by the Mars Regional Atmospheric Modeling System (MRAMS), an atmospheric mesoscale model. A multi-directional wind regime at the local scale is also supported by the observed bimodal distribution of the ripple trends. For the first time, a survey integrating the assessment of dune and ripple migration is presented, showing how dune topography can influence the migration patterns of ripples and how underlying topography appears to control the rates of dune migration.

© 2015 Elsevier Inc. All rights reserved.

1. Introduction and study area

The martian surface has abundant active aeolian bedforms (Fenton, 2006; Bourke et al., 2008) which have been recently observed to migrate in the current climatic setting (Silvestro et al., 2010, 2011, 2013; Chojnacki et al., 2011; Hansen et al., 2011; Bridges et al., 2011, 2012, 2013; Geissler et al., 2013; Sparavigna, 2013). New techniques that take advantage of the high resolution of the HiRISE (High Resolution Imaging Science Experiment) data (McEwen et al., 2007) have been applied to characterize small-scale aeolian bedforms on Mars. The migration rates of ripples were computed using the Coregistration of Optically Sensed Images and Correlation (COSI-Corr) software (Bridges et al., 2012), while ripple trends were automatically derived using the Object-Based Ripple Analysis (OBRA) technique (Silvestro et al., 2011, 2013; Vaz and Silvestro, 2012, 2014).

The aim of this study is to use these two methods in combination to analyze dune and ripple patterns and migration using a pair

of overlapping HiRISE images in Herschel Crater, a 300 km Noachian impact basin in the Mare Tyrrhenium region (MC22) (Fig. 1). The dunes of Herschel are of particular interest as they have been previously interpreted as ancient indurated aeolianites (due to the grooved pattern visible on the dune slopes; Malin and Edgett, 2000). More recent images from the HiRISE camera showed that such a pattern is formed by sand ripples which, together with the dunes, are consistently migrating (Bridges et al., 2007, 2011, 2013). Cardinale et al. (2012a) presented the first evidence for sand motion in Herschel Crater using HiRISE data.

In this work we compute ripple and dune migration rates and compare the migration directions with the present-day winds simulated by the Mars Regional Atmospheric Modeling System (MRAMS), a mesoscale atmospheric model (Michaels and Rafkin, 2008; Rafkin et al., 2001). We use the output of this model to inform and compare with our interpretation of the observed aeolian morphologies. In this way, we also test the capability of the mesoscale climate model to predict the wind regime necessary for the creation and evolution of the Herschel dune fields. We show that the aeolian activity that is shaping the dunes is not strictly unidirectional and that the topography of the crater is controlling the wind flow at the dune field scale.

* Corresponding author at: Dipartimento di Scienze Psicologiche Umanistiche e del Territorio, Università G. d'Annunzio, Via dei Vestini 31, 66100 Chieti, Italy.

E-mail address: marco.cardinale@unich.it (M. Cardinale).

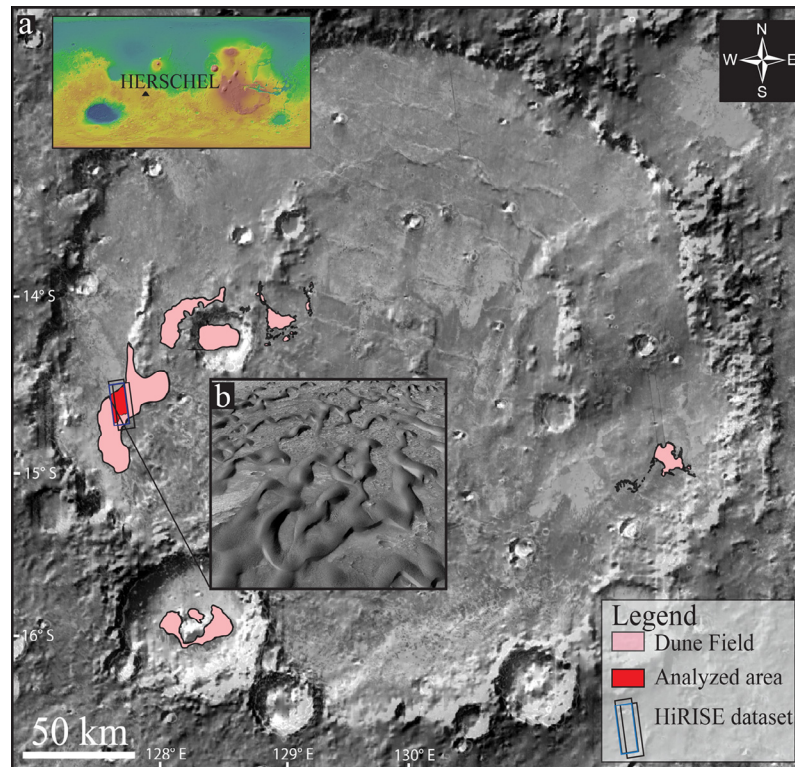


Fig. 1. (a) Details of the study area, showing the distribution of the large dark dune fields within Herschel Crater (MOLA shaded topography with THEMIS daytime mosaic). (b) A perspective view of the large dark dunes from HiRISE images PSP_002860_1650 and ESP_020384_1650. The location of Herschel Crater (Mars Orbiter Laser Altimeter shaded relief) (top left).

Table 1
S1–S2–T3 HiRISE acquisition parameters.

Product ID	S1 PSP_002860_1650	S2 PSP_003572_1650	T3 ESP_020384_1650
Acquisition date	07 March 2007	01 May 2007	01 December 2010
Resolution	0.25 m/pixel	0.25 m/pixel	0.25 m/pixel
Latitude (centered)	−14.807°	−14.805°	−14.813°
Longitude (est)	127.888°	127.890°	127.897°
Local Mars time	3.44 PM	3.22 PM	3.41 PM
Solar longitude	195.9°, Northern autumn	229.7°, Northern autumn	190.9°, Northern autumn
Solar incidence angle	56°	49°	55°
Sub solar azimuth	7.3°	351.4°	9.7°
Emission angle	2.4°	27.3°	4.5°

2. Methods

We conducted a detailed geomorphological analysis of dunes and ripples in Herschel Crater using a time series of HiRISE images and a stereo pair (images S1 and S2) that was used to build a DTM with SOCET SET (Mattson et al., 2011) (Fig. 1, Table 1). Images S1 and T3 (Table 1) were orthorectified over the DTM using the COSI-Corr software package with a window size of 256×256 pixels (Leprince et al., 2007; Bridges et al., 2012).

Dune morphometric parameters (slopes and aspect angles) were computed in ArcGIS and used to derive density stereoplots of the slipface surface vectors, providing an approximation to the main sediment flux direction (Fig. 2d) (Silvestro et al., 2013). Ripple crestlines were mapped over the study dunes in the S1 image using the OBRA procedure introduced by Vaz and Silvestro (2014). This technique is used to derive the main trends of the

ripples, providing information about wind/sediment interactions at smaller scales (Fig. 3).

The lee fronts of the dune slipfaces were manually digitized on the S1 and T3 images in order to derive the dune migration rate and direction (Fig. 4). In addition, we also evaluated the spatial distribution of the dune migration azimuth (Fig. 5). We then used COSI-Corr to track the ripple displacement over the S1 and T3 images acquired 1359 Earth-days apart (Table 1). The result is a ripple displacement map (Fig. 6) from which we derived the average ripple migration rate (Figs. 7 and 8). The displacement map was obtained by using the statistical correlator in COSI-Corr, setting a window size of 70 pixels with a step of 16 pixels. The same tuning parameters have been used to track the ripple displacement in Nili Patera (Bridges et al., 2012, supplementary information).

Finally, we estimated the potential timing of the sand-moving events by using the MRAMS model results from two different grid

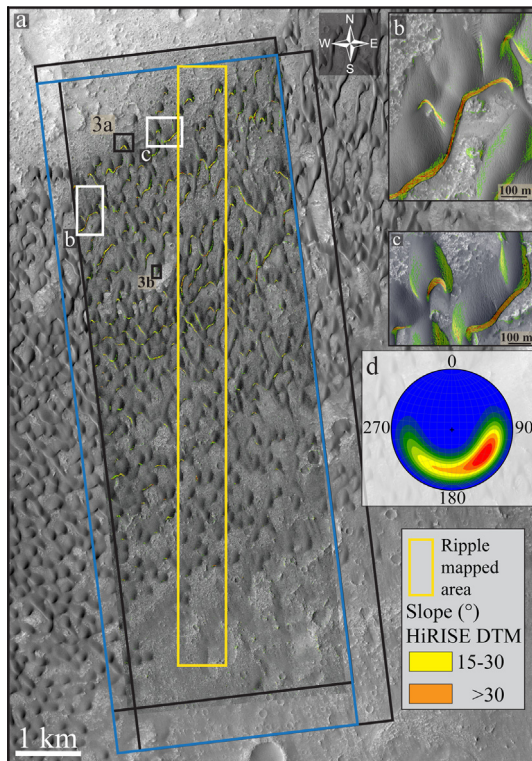


Fig. 2. (a) The Herschel Crater dune field (CTX image P05_002860_1650_XI_15S232W) slope map derived from High Resolution Imaging Science Experiment digital terrain models (DTMs). (b and c) Barchan dunes with and without elongated horns in the northern and north-eastern area of the dune field. The slope map suggests the presence of a slipface trend of 62–286°, denoting a predominant wind direction blowing from the northwest (HiRISE image PSP_002860_1650). (d) The lower hemisphere equal-area density stereonet for all the slipface surface vectors estimated from the HiRISE DTMs. The estimated dip angle is $\sim 30^\circ$.

scales (the two highest-resolution members of a telescoping set of 5 grids). For each season the model was run for 4 sols, and instantaneous snapshots of the model fields were recorded every twenty Mars-minutes. Fig. 9 illustrates a selection of metrics derived from the surface stress and wind direction fields from one typical day for each of the four seasons at $L_s = 210^\circ$, 300° , 30° and 120° (corresponding to southern spring, summer, autumn, and winter, respectively; using results with ~ 8 -km grid spacing). An additional way of visualizing the MRAMS results (using results with ~ 2 -km grid spacing) is shown for the area of the HiRISE images used for this investigation (Fig. 10). The modeled winds have been sorted into 24 equal-width direction bins of 15° over the dune field. Each point may have a maximum of 24 vectors, which represent the downwind direction. These plots (Figs. 10–12) contain MRAMS results for 12 seasons: at $L_s = 0^\circ$, 30° , 60° (southern autumn), $L_s = 90^\circ$, 120° , 150° (southern winter), $L_s = 180^\circ$, 210° , 240° (southern spring), $L_s = 270^\circ$, 300° , 330° (southern summer). A ratio defined as the aerodynamic surface stress divided by the minimum fluid threshold aerodynamic stress calculated using the expressions of Greeley and Iversen (1985) is used to assess potential wind sediment transport.

3. Dune and ripple morphology

The study dunes are located in a $\sim 1200 \text{ km}^2$ dune field in the western floor of Herschel Crater, and consist of barchans and barchanoids (Cardinale et al., 2012b). These dunes can be more than 60 m tall and are spaced ~ 200 – 800 m apart. Some of the

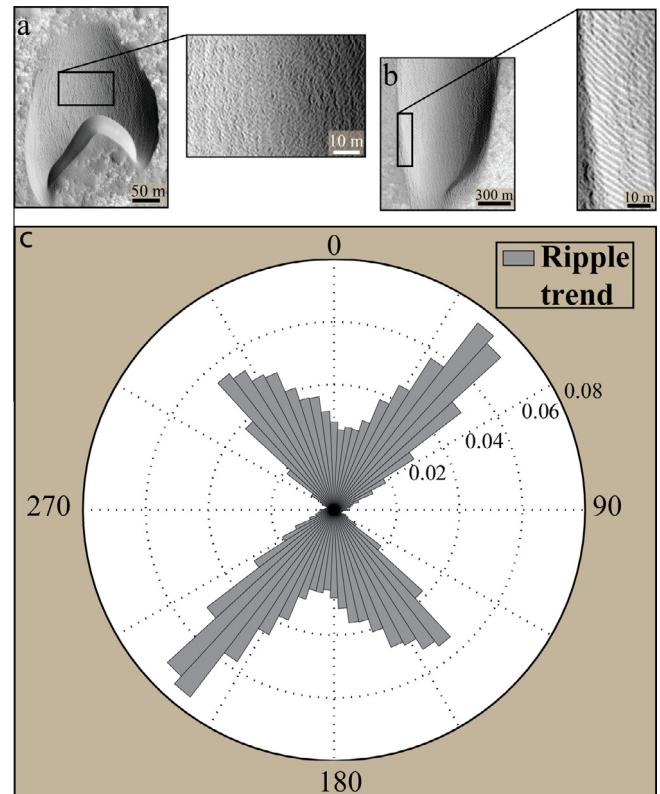


Fig. 3. (a) The pattern of the ripples superposing the dune slopes is complex due to the diverse wind flow over the dunes. (b) An inset of dune horn, where along its flanks, the ripple crests present a continuous pattern. (c) Ripple length-weighted distribution in Herschel Crater (the relative frequency for each 5° bin is shown). The ripple population (the mapped area corresponds to the yellow window shown in Fig. 2) denotes a bimodal trend with two prevailing directions centered at $\sim 45^\circ$ and $\sim 135^\circ$. (For interpretation of the references to color in this figure legend, the reader is referred to the web version of this article.)

dunes present an asymmetric structure, with an oblique elongation of the slip faces (Fig. 2b and c). Visual assessment and stereonet analysis reveal that slipface slope values cluster at $\sim 30^\circ$, while their orientation presents a high dispersion (Fig. 2d). Most of the slipface vectors are oriented toward the south, trending between $\sim 60^\circ$ and $\sim 300^\circ$ with a dominant direction centered around $\sim 125^\circ$ (Fig. 2d), reflecting the dune slipface asymmetry.

In Fig. 3 we show some examples of the different types of ripple patterns in the area. On the dune flanks, ripples are spaced 2–4 m apart and are two-dimensional (Rubin, 2012) (continuous and forming a regular pattern) with typical “Y” junction terminations (Fig. 3a). However, on the top of the dunes the ripple pattern is more three-dimensional (complex), with diverse ripple sets overlapping (Fig. 3b). Such a ripple arrangement probably reflects the coupling between ripple straightness and slope (the higher the slope, the straighter the ripple) described by Rubin (2012) and observed in the field by Howard (1977). The complexity of the ripple pattern is shown in the rose diagram in Fig. 3c (showing the distribution of the crestline trends mapped automatically over the dunes in the yellow box of the Fig. 3a). The length-weighted circular distribution of the mapped ripple crests is bimodal, with dominant directions centered around $\sim 45^\circ$ and $\sim 135^\circ$.

4. Bedform migration

4.1. Dunes

In Fig. 4a we show the spatial distribution of the average dune migration vectors for 211 dunes computed by comparing the

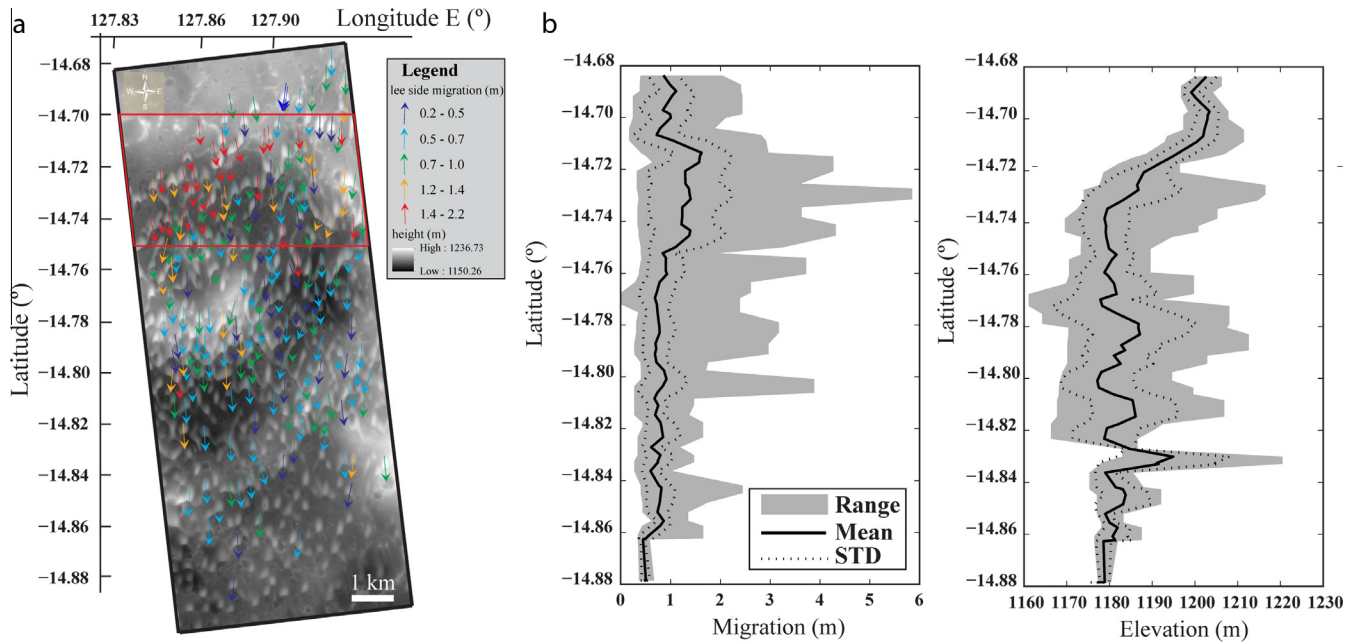


Fig. 4. (a) Average dune lee front migration vectors overlain on the DTM. The colored vectors represent the average displacement of the slipface lee fronts over three Earth-years (from March 2007 to December 2010). (b and c) The plots represent the statistics computed using 500 m moving windows for the migration and elevation at the base of the slipfaces. Note the general decrease of the displacements when moving south, and the association of the area with larger migrations (between -14.7° and -14.75°) with a drop in elevation. (For interpretation of the references to color in this figure legend, the reader is referred to the web version of this article.)

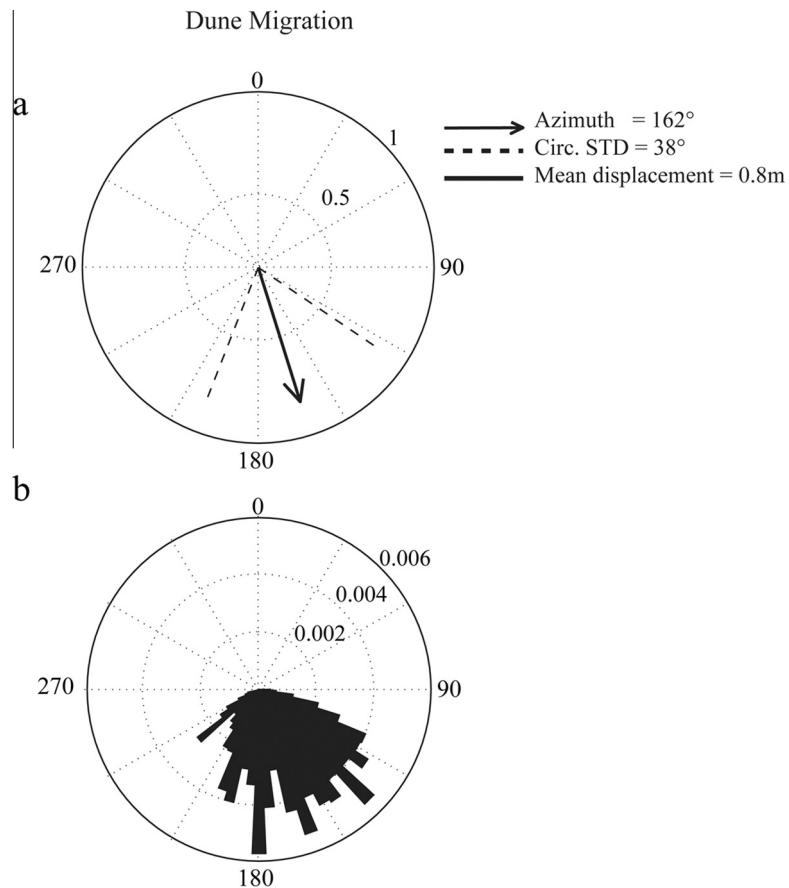


Fig. 5. Circular distribution of the lee side migration vectors at this Herschel Crater site. (a) Mean vector of the lee side migration (dashed lines represent the circular standard deviation interval; distances from the center of the plot are in meters). (b) Circular distribution of the vectors used to compute the mean vector (the presented relative frequencies correspond to bin sizes of 5°).

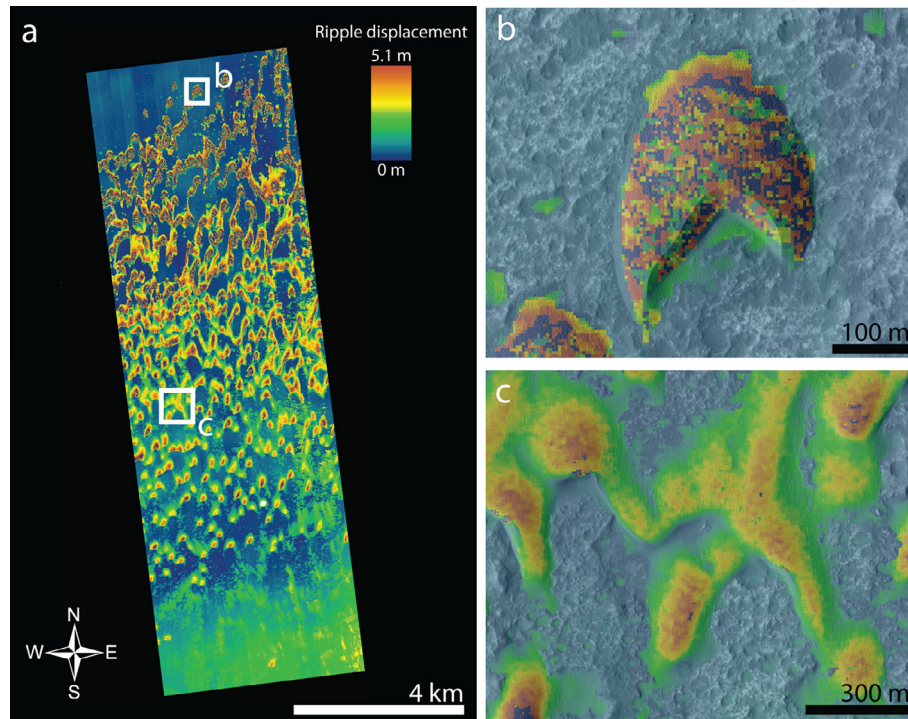


Fig. 6. Ripple displacement map for the Herschel Crater dune field derived from correlated HiRISE images, with high displacements shown with warmer colors. (b) Some ripples moved so much that the correlation broke down causing the observed fuzzy pattern. (c) Area in which the correlation starts to record the ripple migration. (For interpretation of the references to color in this figure legend, the reader is referred to the web version of this article.)

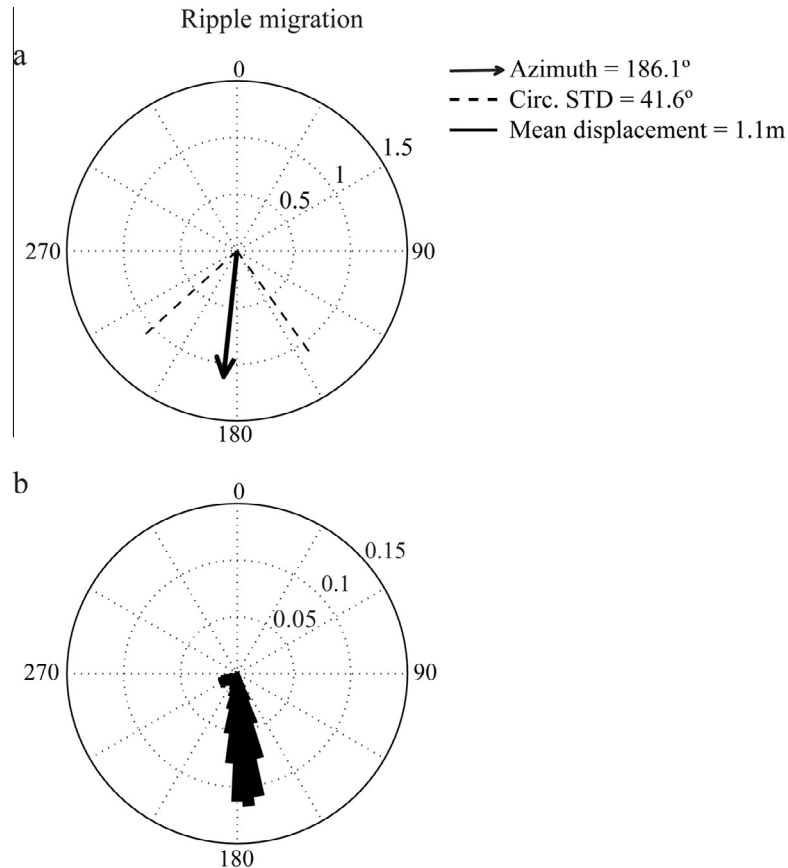


Fig. 7. Circular distribution of the ripple migration vectors in Herschel Crater. (a) Ripple migration mean vector (dashed lines represent the circular standard deviation interval; distances from the center of the plot are in meters). (b) Circular distribution of the vectors used to compute the mean vector (the presented relative frequencies correspond to bin sizes of 5°). The secondary dominant direction centered around ~240° is due to the ripple migration vectors in the lee of the dunes (see Fig. 8).

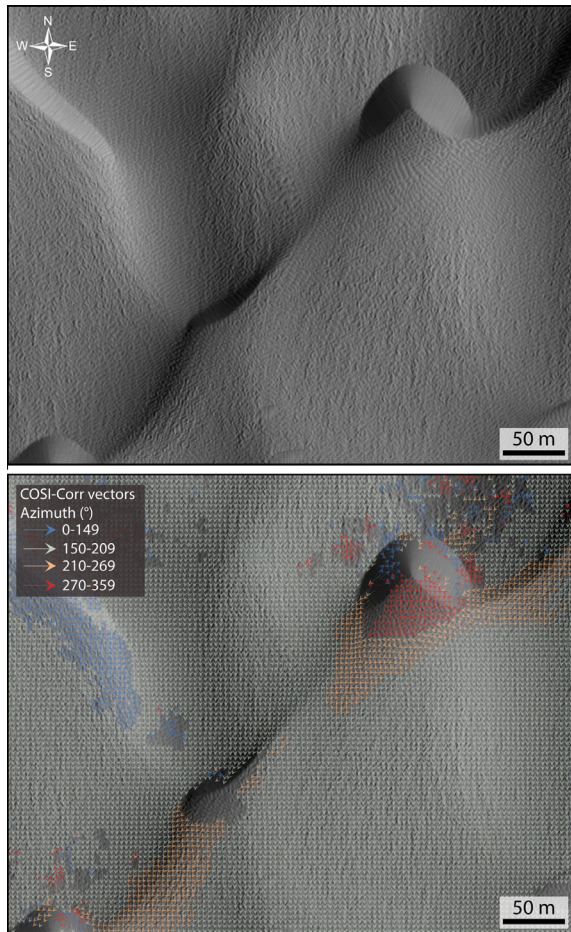


Fig. 8. COSI-Corr vectors showing the magnitude and trend of ripple migration. On the lee side of the dunes, ripple migration vectors are deflected toward the SSW.

HiRISE image pair S1 and T3 (Table 1) ($\Delta t = 1359$ Earth-days). Dunes that do not have a clear slipface are excluded from the analysis. The distribution of the lee motion is neither uniform nor unidirectional (Fig. 5). A higher migration value is reported for the dunes located in the northern dune field sector (1.2–2.2 m), with the dune displacements decreasing toward the south (Fig. 4a). The graphs in Fig. 4b highlight the north–south spatial variation of dune migration (left), and shows that the area with larger migration values (between -14.70° and -14.75° in latitude) corresponds to a drop in elevation that is well represented in the northern part of the Herschel dune field (right). Apart from this peak, migration rates decrease consistently southward.

On average, the dunes migrated 0.8 m toward the SSE (Fig. 5a shows the computed average vector) giving a rate of migration of 0.45 m/Mars-year (m/MY) (~ 0.2 m/Earth-year or m/EY), assuming that this value remains constant from year to year. The measurements show high directional dispersion around the mean ($\mu = 162^\circ \pm 38^\circ$) (Fig. 5b), which might be partially due to the local topography, since the dunes are not migrating across a flat surface.

4.2. Ripples

In Fig. 6 we show the ripple displacement map obtained with COSI-Corr. The map reveals that significant movement occurred

across the investigated area between March 2007 and December 2010. In the northern area of the Herschel dune field, the fastest ripples moved so far that the correlation breaks down once the migration exceeds a distance greater than or equal to the ripple wavelength (5.1 m) (Fig. 6b). In the central and southern dune field sectors the ripple displacement decreases, so it can be traced (Fig. 6a and c). The ripple migration rate also varies with the height of the dunes, with the fastest-migrating ripples located close to the dune crests (Fig. 6c). This is the result of the linear relationship between height and ripple migration that has also been reported for dunes in Nili Patera and Gale Crater (Bridges et al., 2012; Vaz and Silvestro, 2014). During a period of 1359 Earth-days we obtained an average vector for ripple migration of 1.1 m trending at 186.1° (Fig. 7a). This gives an average migration rate of 0.55 m in one MY (~ 0.3 m/EY). In addition, the circular plot in Fig. 7b shows that the migration vectors present a bimodal circular distribution, with a primary mode trending $\sim 175^\circ$ (similar to the average dune migration vector in Fig. 2a) and a secondary mode trending $\sim 240^\circ$. This bimodality results in a high directional dispersion of the ripple migration vectors (circular standard deviation of 41.6°), and is probably related to dune topography, which deflects the wind over the dunes as shown in Fig. 8. In particular, the secondary dominant direction centered on $\sim 240^\circ$ is due to the ripple migration vectors in the lee of the dunes (orange¹ vectors in Fig. 8).

5. Modeled winds

The atmospheric model (MRAMS) results are used to evaluate wind strength and direction, in order to try to explain the observed aeolian morphologies and dune changes (Fenton et al., 2005; Hayward et al., 2007; Chojnacki et al., 2011). In Fig. 9a and b (8-km grid spacing) we show the mean wind stress ratio (stress/threshold stress) vectors over the entire dune field. This coarser-resolution grid is useful to look at the regional winds (not shown). The dominant modeled mean wind direction is from the west to the east (Fig. 9c) with the strongest winds blowing near the western crater rim (Fig. 9a). The predicted stress values are just above the Kok (2010) impact threshold for sand saltation maintenance, which is $\sim 10\%$ of the Greeley and Iversen (1985) fluid threshold (at which saltation initiates). In Fig. 9b we show the directional variability of the modeled winds, as represented by the circular standard deviation. A general trend is visible with the winds being more uni-directional near the western crater rim (see the lower circular standard deviation in this area and Table 2). In Fig. 9d we show the same data plotted by season, with the relevant statistic parameters summarized in Table 2. The strongest winds blow at $L_s = 30^\circ$ (southern autumn) from the west to the east with a circular standard deviation of 34° . In the other seasons modeled winds are weaker and multi-directional (circular standard deviation $> 87^\circ$). Frequent winds from the north to the south, matching the dune and ripple migration direction, are not predicted by the model.

Output from MRAMS at 2-km grid scale (Fig. 10) may better resolve local winds relevant to dune and ripple migration. Additionally, mean winds are not calculated/used in the analysis illustrated in Figs. 10–12. This is because the aeolian modification observed may be due to infrequent strong winds (with much weaker winds the remainder of the time). A strong, but infrequent wind from the N–NE (better matching the observed dune and ripple migration) is visible within the study area (Fig. 10; contains winds from 12 seasons). To determine which season(s) this wind

¹ For interpretation of color in Fig. 8, the reader is referred to the web version of this article.

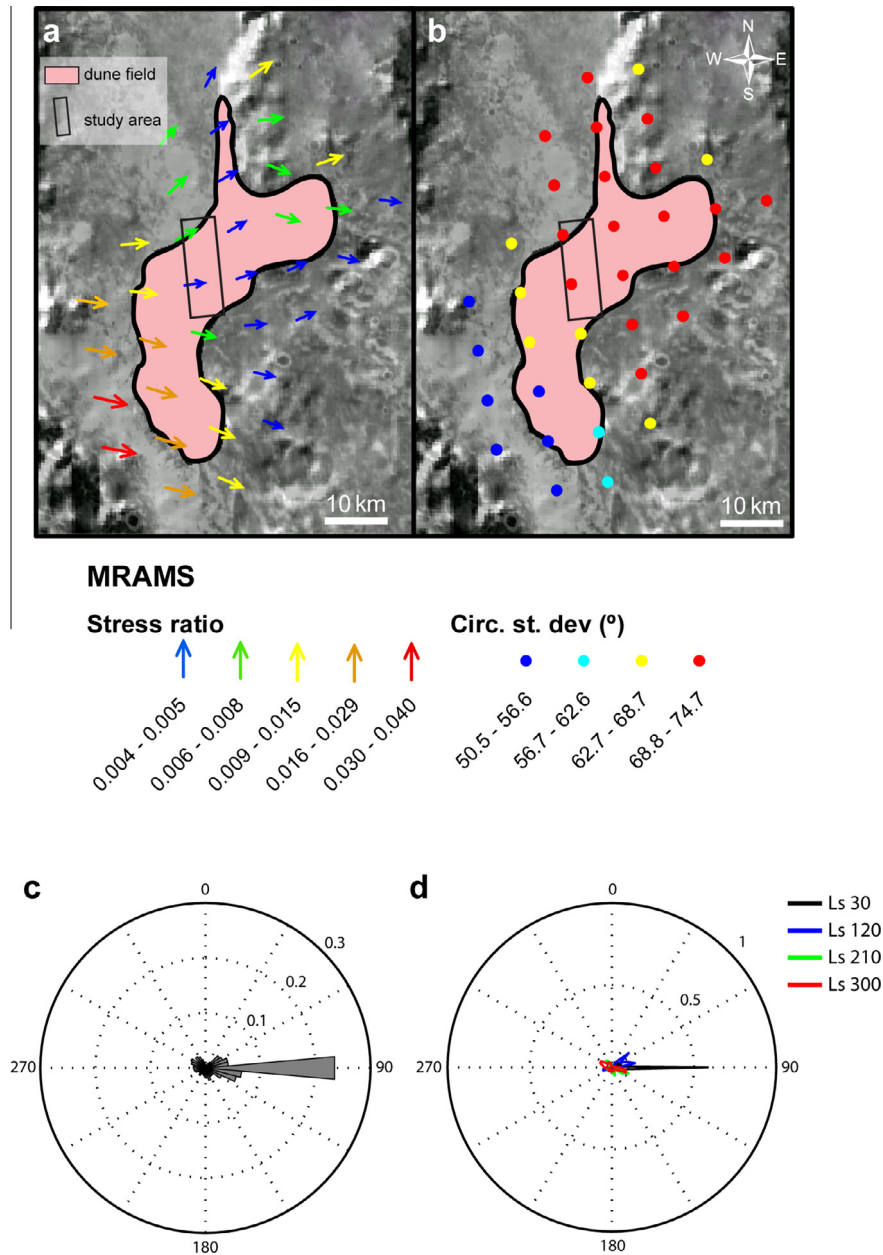


Fig. 9. Metrics derived from modeled wind stresses and directions. (a) Mean stress ratio vectors for each of the 36 model nodes covering the dune field. The azimuth of the vectors corresponds to the wind direction, while the color is the ratio between the modeled aerodynamic surface stress and the aerodynamic fluid threshold stress (Greeley and Iversen, 1985). (b) Circular standard deviation associated with the mean vectors shown in (a). (c) Circular distribution of the wind stress ratio vectors. (d) Circular distribution of the wind stress ratio vectors plotted for each season. The circular frequencies plotted in (c) and (d) were computed using angular bins, each 5° in width. (For interpretation of the references to color in this figure legend, the reader is referred to the web version of this article.)

regime occurs in, Fig. 11 shows the wind stress ratio (radial grid) vs. wind direction for each of 12 seasons throughout a Mars-year – including only the grid points within the HiRISE image footprint (see Fig. 10). The wind regime from the N–NE is active in southern summer and early autumn (L_s 270–0°), peaking in strength at around $L_s = 330^\circ$ (late southern summer). Other weaker wind regimes are also evident throughout the year, including some that appear to align with the secondary ripple trend (Fig. 3c). The maximum simulated wind stress ratio values are three times greater than the impact threshold for sand saltation (Kok, 2010) (Figs. 11 and 12).

6. Discussion

The detected southward migration of dunes and ripples indicates that the dune field in Herschel Crater is shaped by dominant winds blowing from the north. However, asymmetry in the dune form indicates that the wind regime is not strictly uni-directional (Bourke, 2009; Parteli et al., 2014). In particular, following the model of Bagnold (1941), the influence of a local bimodal wind regime with winds blowing from NNW and from NNE, should be the cause for the observed asymmetry. In the study area the NNW winds should be more frequent and/or stronger

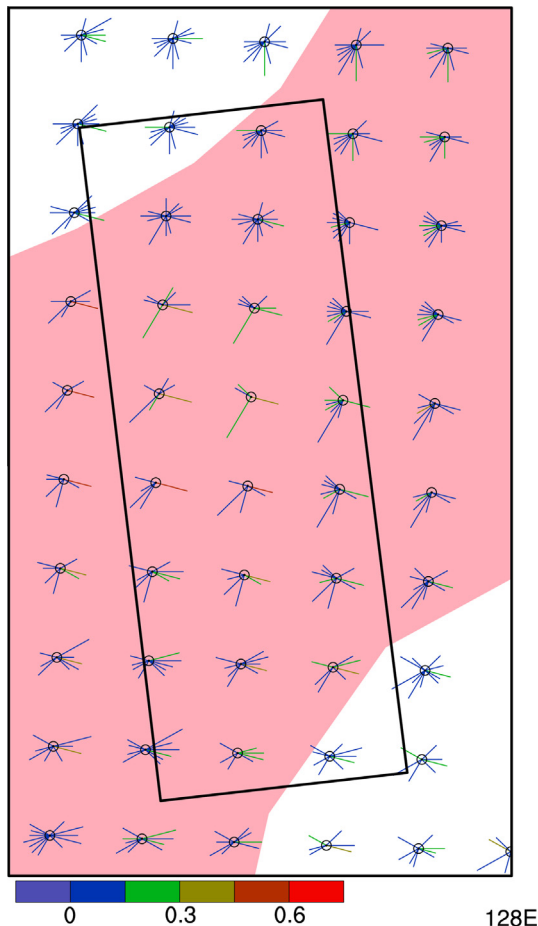


Fig. 10. MRAMS wind metrics over the studied dune field, including 12 seasons (an entire year). The pink shaded area shows the dune field location. The black window indicates the HiRISE image coverage. Only winds >10% of the Greeley and Iversen (1985) fluid threshold for saltation are included in this plot. Each vector shows the downwind direction of the wind (the direction of the wind is flowing toward). The length of each vector is proportional to the greatest wind stress ratio (between the model aerodynamic surface stress and the aerodynamic fluid threshold stress) at each of 24 possible direction bins, while the color shows the relative frequency of each wind direction at each point (warmer colors correspond to more frequent winds blowing in that direction). (For interpretation of the references to color in this figure legend, the reader is referred to the web version of this article.)

(Fig. 2b and c). Ripples are bedforms that evolve faster, better reflecting local-scale, short-period wind dynamics. Even so, the overall bimodal distribution of their trends also suggests a non-unimodal wind scenario at the local scale.

The Herschel dunes and ripples display spatial variations in their migration rates. Ripple and dune migration rates decrease southward, while the drop in elevation (20 m) between -14.70° and -14.74° (latitude; highlighted in Fig. 4b) appears associated with a peak in the dune migration rate. On Earth, spatial variations in the sediment flux and dune morphology have been observed at White Sands (New Mexico, USA) and explained by the development of an internal boundary layer (IBL) (Jerolmack et al., 2012), controlled by roughness variations under the influence of underlying long-wavelength topography (Pelletier, 2014). In the study area, the N–S variations in the dune and ripple migration suggests that the same mechanisms are likely implicated (see the peak of dune migration between -14.70° and -14.74° latitude, highlighted in Fig. 4b). However, the complexity of the topography and the nature of our measurements (bedform migration rates instead of sand fluxes) hinder any robust conclusion regarding

the relative weight of roughness transitions and long-wavelength topography.

There is a clear discrepancy between the arithmetic mean wind (Fig. 9a) and a more detailed analysis at higher spatial resolution that concentrates on only the winds most capable of moving sediment (even if they are infrequent; Figs. 10–12). In this particular location, part of the difference is likely due to better-resolved topography and its interaction with the atmosphere. However, if the aeolian modification observed is due to infrequent strong winds, with much weaker winds the remainder of the time (and/or other strong winds from significantly different directions), the mean wind will be misleading.

The higher-resolution MRAMS results do predict strong winds from the north and northwest, qualitatively matching bedform migration and ripple trends. Additionally, the diverse seasonal wind regimes (Figs. 11 and 12) may partially explain the intricate ripple pattern. However, observations of dune and ripple migration indicate that the north wind regime is significantly more effective (strong) than any other wind regime – a detail that the model results do not capture. The ripple migration direction also appears to be controlled by winds that are topographically deflected by the dune slopes, and any extrapolation from local to dune field/regional scale has to be treated carefully. The lower spatial resolution (compared to the individual dunes) and temporal coverage (every sol of the year is not included) of the mesoscale climate simulations is dictated primarily by the significant computational time required. A similar situation has also been reported by other workers (Hayward et al., 2009; Silvestro et al., 2012), suggesting the importance of ground truth data when determining wind regimes on Mars at fine spatiotemporal resolutions.

With the exception of the Nili Patera ripples which migrate unusually fast (Silvestro et al., 2010; Bridges et al., 2012), bedform migration rates in Herschel appear to be comparable to other areas on Mars (Silvestro et al., 2011, 2013). However, without continuous and long-term monitoring of Herschel and other zones of known aeolian activity, this comparison remains speculative.

7. Conclusion

The high spatial resolution of HiRISE images, combined with COSI-Corr and MRAMS simulations, allowed us to quantify dune and ripple displacement rates and better constrain the wind complexity in Herschel Crater. During the analyzed time period, dunes have migrated at an average rate of 0.45 m/MY (~ 0.2 m/EY), while ripples migrated 0.55 m/MY (~ 0.3 m/EY). On average, dunes and ripples migrated southward (162° and 175° respectively), although significant trend and magnitude variations were recognized.

At the dune field scale, we have shown that the change in the roughness represented by the northern dune field edge combined with a drop in elevation of the underlying bedrock appear to control bedform migration rates. Our results show that regional and local topographic settings are indeed an important boundary condition that needs to be carefully addressed in order to explain spatial variations in the migration rates and morphologies of dunes and ripples.

Finally, the MRAMS modeling results exhibit both strong winds from north and from the northwest, broadly consistent with the observed dune and ripple morphologies. The modeling does not indicate a clear dominance of the winds from the north over the other wind regimes, unlike what was observationally inferred from bedform migration. Influence of local dune topography (not resolved by the model) on the winds may explain some of this difference.

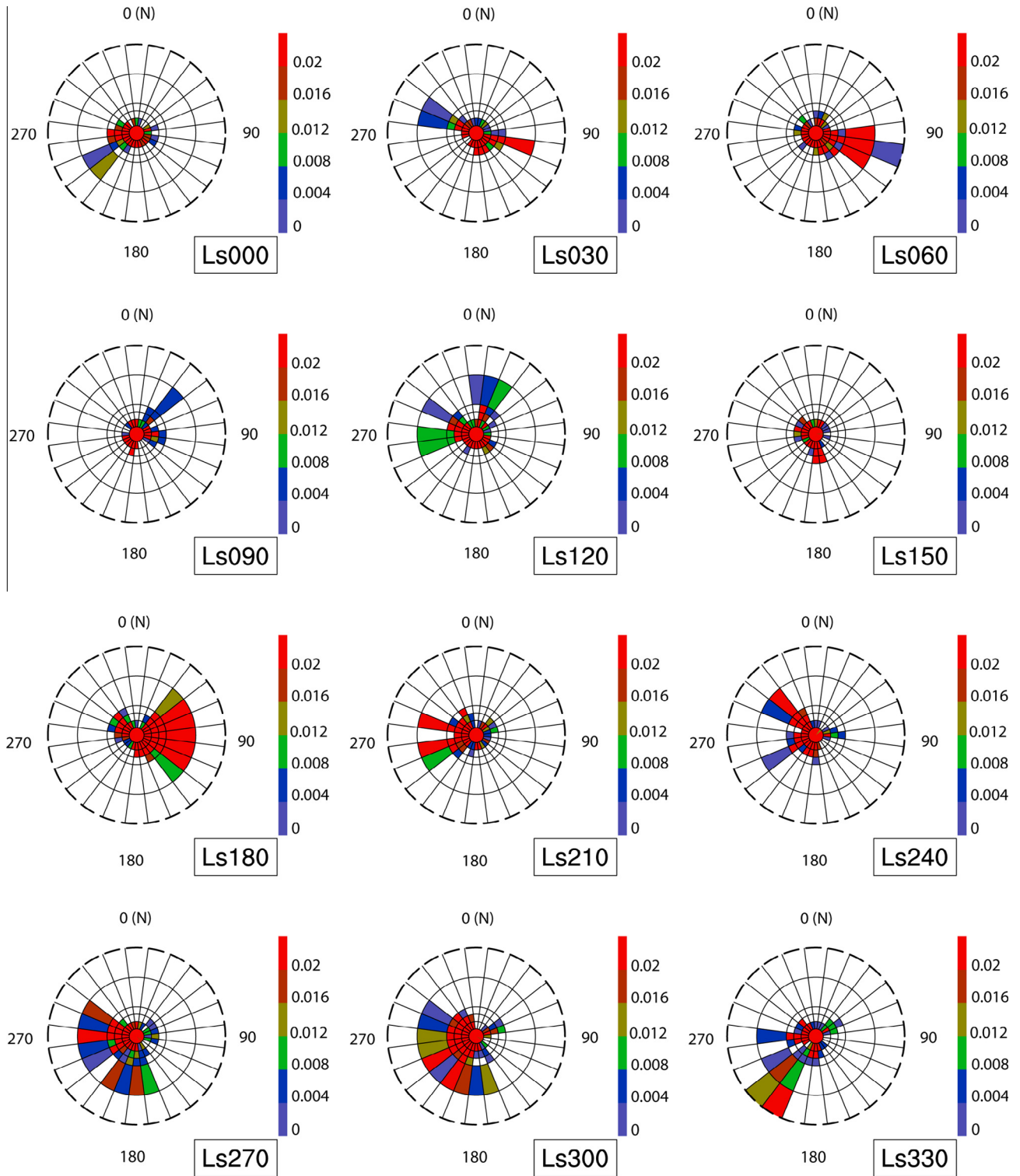


Fig. 11. Seasonal wind regimes, as modeled by MRAMS. Each polar plot contains the combined information of all MRAMS grid points within the HiRISE image outline (see Fig. 10), for all 12 seasons (an entire year). In these plots, the radial direction is the wind stress ratio (stress/fluid threshold stress), with the outer ring having a value of 0.3 and the center of each plot being zero. The azimuthal coordinate is direction (that the wind is blowing toward). Each bin is colored by the relative frequency of each wind direction/magnitude (warmer colors correspond to more frequent winds blowing in that direction and at that magnitude). (For interpretation of the references to color in this figure legend, the reader is referred to the web version of this article.)

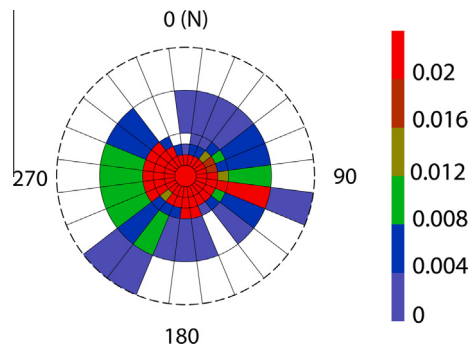


Fig. 12. Annual modeled wind regime. The plot shows the sum of all 12 seasons, for all MRAMS grid points within the HiRISE image outline (see Fig. 10). In this plot, the radial direction is the wind stress ratio (stress/fluid threshold stress), with the outer ring having a value of 0.3 and the center of each plot being zero. The azimuthal coordinate is direction (that the wind is blowing toward). Each bin is colored by the relative frequency of each wind direction/magnitude (warmer colors correspond to more frequent winds blowing in that direction). (For interpretation of the references to color in this figure legend, the reader is referred to the web version of this article.)

Table 2

Statistical parameters of the modeled winds, divided by season.

Solar longitude	Mean azimuth	Circular standard deviation
30°	88.72726°	33.93312
120°	67.86047°	86.73132
210°	145.4258°	103.0098
300°	232.3831°	120.6203

Acknowledgments

M. Cardinale is supported by a grant from the ASI (Agenzia Spaziale Italiana). S. Silvestro is supported by ASI through the ASI-CISAS agreement I/018/12/0: “DREAMS EDM Payload—ExoMars 2016”. D. Vaz was supported by FCT (Fundação para a Ciência e a Tecnologia) with the grant FRH/BPD/72371/2010. We thank two anonymous reviewers and the journal editor for useful advice and comments.

References

Bagnold, R.A., 1941. *The Physics of Blown Sand and Desert Dunes*. Methuen, London, 265 pp.

Bourke, M.C., 2009. Barchan dune asymmetry: Observations from Mars and Earth. *Icarus* 205, 183–197. <http://dx.doi.org/10.1016/j.icarus.2009.08.023>.

Bourke, M.C., Edgett, K.S., Cantor, B.A., 2008. Recent aeolian dune change on Mars. *Geomorphology* 94, 247–255. <http://dx.doi.org/10.1016/j.geomorph.2007.05.012>.

Bridges, N.T. et al., 2007. Windy Mars: A dynamic planet as seen by the HiRISE camera. *Geophys. Res. Lett.* 34, L23205. <http://dx.doi.org/10.1029/2007GL031445>.

Bridges, N.T. et al., 2011. Planet-wide sand motion on Mars. *Geology* 40 (January 2012), 31–34. <http://dx.doi.org/10.1130/G32373.1> (first published on November 14, 2011).

Bridges, N.T. et al., 2012. Earth-like sand fluxes on Mars. *Nature* 485 (7398), 339–342. <http://dx.doi.org/10.1038/nature11022>.

Bridges, N. et al., 2013. Bedform migration on Mars: Current results and future plans. *Aeolian Res.* <http://dx.doi.org/10.1016/j.aeolia.2013.02.004>.

Cardinale, M. et al., 2012a. Evidences for sand motion in the equatorial region of Mars. *Lunar Planet. Sci.* 43, LPI Contribution No. 1659, id. 2452.

Cardinale, M. et al., 2012b. The influence of local topography for wind direction on Mars: Two examples of dune fields in crater basins. *Earth Surf. Process. Landforms* 37, 1437–1443. <http://dx.doi.org/10.1002/esp.3289>.

Chojnacki, M. et al., 2011. Orbital observations of contemporary dune activity in Endeavour Crater, Meridiani Planum, Mars. *J. Geophys. Res.* 116, E00F19. <http://dx.doi.org/10.1029/2010JE003675>.

Fenton, L.K., 2006. Dune migration and slip face advancement in the Rabe Crater dune field, Mars. *Geophys. Res. Lett.* 33, L20201. <http://dx.doi.org/10.1029/2006GL027133>.

Fenton, L.K., Toigo, A.D., Richardson, M.I., 2005. Aeolian processes in Proctor Crater on Mars: Mesoscale modelling on dune-forming winds. *J. Geophys. Res.* 110, E06005. <http://dx.doi.org/10.1029/2004JE002309>.

Geissler, P.E. et al., 2013. Shifting sands on Mars: Insights from tropical intra-crater dunes. *Earth Surf. Process. Landforms* 38, 407–412. <http://dx.doi.org/10.1002/esp.3331>.

Greeley, R., Iversen, J.D., 1985. *Wind as a geological process on Earth, Mars, Venus and Titan*. In: *Cambridge Planetary Science Series No. 4*. Cambridge University Press, Cambridge, London, New York, New Rochelle, Melbourne, Sydney, xii + 333 pp.

Hansen, C.J. et al., 2011. Seasonal erosion and restoration of Mars northern polar dunes. *Science* 331, 575–578. <http://dx.doi.org/10.1126/science.1197636>.

Hayward, R.K. et al., 2007. Mars Global Digital Dune Database and initial science results. *J. Geophys. Res.* 112, E11007. <http://dx.doi.org/10.1029/2007JE002943>.

Hayward, R.K. et al., 2009. Aeolian dunes as ground truth for atmospheric modeling on Mars. *J. Geophys. Res.* 114, E11012. <http://dx.doi.org/10.1029/2009JE003428>.

Howard, H.D., 1977. Effect of slope on the threshold of motion and its application to orientation of wind ripples. *Geol. Soc. Am. Bull.* 88, 853–856.

Jerolmack, D.J. et al., 2012. Internal boundary layer model for the evolution of desert dune fields. *Nat. Geosci.* 5, 206–209. <http://dx.doi.org/10.1038/ngeo1381>.

Kok, J.F., 2010. An improved parameterization of wind-blown sand flux on Mars that include the effect of hysteresis. *Geophys. Res. Lett.* 37, L12202. <http://dx.doi.org/10.1029/2010GL043646>.

Leprince, S. et al., 2007. Automatic and precise ortho-rectification, coregistration, and subpixel correlation of satellite images, application to ground deformation measurements. *IEEE Trans. Geosci. Remote Sens.* 45 (6), 1529–1558.

Malin, M.C., Edgett, K.S., 2000. Sedimentary rocks of early Mars. *Science* 290, 1927–1937. <http://dx.doi.org/10.1126/science.290.5498.1927>.

Mattson, S. et al., 2011. Release of HiRISE digital terrain models to the planetary data system. *Lunar Planet. Sci.* 42. Lunar and Planetary Institute Contribution 1608, The Woodlands, Texas, p. 1558.

McEwen, A.S. et al., 2007. Mars reconnaissance orbiter's High Resolution Imaging Science Experiment (HiRISE). *J. Geophys. Res.* 112, E05S02. <http://dx.doi.org/10.1029/2005JE002605>.

Michaels, T.I., Rafkin, S.C.R., 2008. Meteorological predictions for candidate 2007 Phoenix Mars Lander sites using the Mars Regional Atmospheric Modeling System (MRAMS). *J. Geophys. Res.* 113, E00A07. <http://dx.doi.org/10.1029/2007JE003013>.

Parteli, E.J.R. et al., 2014. Origins of barchan dune asymmetry: Insights from numerical simulations. *Aeolian Res.* 12, 121–133. <http://dx.doi.org/10.1016/j.aeolia.2013.12.002>, ISSN 1875-9637.

Pelletier, J.D., 2014. Controls on the large-scale spatial variations of dune-field properties in the barchanoid portion of White Sands dune field, New Mexico. *J. Geophys. Res.* *Earth Surf.* <http://dx.doi.org/10.1002/2014JF003314>.

Rafkin, S.C.R., Haberle, R.M., Michaels, T.I., 2001. The Mars Regional Atmospheric Modeling System: Model description and selected simulations. *Icarus* 151, 228–256. <http://dx.doi.org/10.1006/icar.2001.6605>.

Rubin, D.M., 2012. A unifying model for platform straightness of ripples and dunes in air and water. In: *Third International Planetary Dunes Workshop: Remote Sensing and Image Analysis of Planetary Dunes*. Flagstaff, Arizona, Abstract #7020.

Silvestro, S., Fenton, L.K., Vaz, D.A., Bridges, N.T., Ori, G.G., 2010. Ripple migration and dune activity on Mars: Evidence for dynamic wind processes. *Geophys. Res. Lett.* 37, L20203. <http://dx.doi.org/10.1029/2010GL044743>.

Silvestro, S. et al., 2011. Active eolian processes on Mars: A regional study in Arabia and Meridiani Terrae. *Geophys. Res. Lett.* 38, L20201. <http://dx.doi.org/10.1029/2011GL048955>.

Silvestro, S. et al., 2012. Interpretation of the complex dune morphology on Mars: Dune activity, modelling and a terrestrial analogue. *Earth Surf. Process. Landforms* 37, 1424–1436. <http://dx.doi.org/10.1002/esp.3286>.

Silvestro, S. et al., 2013. Pervasive aeolian activity along rover Curiosity's traverse in Gale Crater, Mars. *Geology* 2013. <http://dx.doi.org/10.1130/G34162.1>.

Sparavigna, Amelia Carolina, 2013. Edge-detection applied to moving sand dunes on Mars. Available from arXiv:1308.5315.

Vaz, D.A., Silvestro, S., 2012. An object based approach for the mapping and characterization of Mars ripples. In: *The Third International Planetary Dunes Workshop: Remote Sensing and Image Analysis of Planetary Dunes*. Flagstaff, AZ, USA, Abstract #7019.

Vaz, D.A., Silvestro, S., 2014. Mapping and characterization of small-scale aeolian structures on Mars: An example from the MSL landing site in Gale Crater. *Icarus* 230, 151–161. <http://dx.doi.org/10.1016/j.icarus.2013.08.007>.